

# Majorana Kramers pairs in higher-order topological insulators

Chen-Hsuan Hsu<sup>1</sup>, Peter Stano<sup>1,2,3</sup>, Jelena Klinovaja<sup>1,4</sup>, and Daniel Loss<sup>1,4</sup>

<sup>1</sup>*RIKEN Center for Emergent Matter Science (CEMS), Wako, Saitama 351-0198, Japan*

<sup>2</sup>*Department of Applied Physics, School of Engineering,*

*University of Tokyo, 7-3-1 Hongo, Bunkyo-ku, Tokyo 113-8656, Japan*

<sup>3</sup>*Institute of Physics, Slovak Academy of Sciences, 845 11 Bratislava, Slovakia and*

<sup>4</sup>*Department of Physics, University of Basel, Klingelbergstrasse 82, CH-4056 Basel, Switzerland*

(Dated: September 27, 2018)

We propose a tune-free scheme to realize Kramers pairs of Majorana bound states in recently discovered higher-order topological insulators (HOTIs). We show that, by bringing two hinges of a HOTI into the proximity of an  $s$ -wave superconductor, the competition between local and crossed Andreev pairing leads to formation of Majorana Kramers pairs, when the latter pairing dominates over the former. We demonstrate that such a topological superconductivity is stabilized by moderate electron-electron interactions. The proposed setup avoids the application of a magnetic field or local voltage gates, and requires weaker interactions comparing to nonhelical nanowires.

Majorana bound states, being prospects of topological quantum computation, have gained much attention in the past decades [1–31]. However, the paradigm setup for their realization in semiconducting nanowires with strong spin-orbit interaction and proximity-induced superconductivity [32–44] requires the application of an external magnetic field, which suppresses the superconducting gap and is therefore detrimental to the Majorana bound states themselves.

Alternative routes are taken to seek for the Majorana bound states without an external magnetic field [45–51], including spontaneous helical spin textures [52–59] and crossed Andreev pairing process in double nanowires or the edge channels of two-dimensional topological insulators [60–66]. In the former setup the spin texture is stabilized by an indirect coupling mediated by itinerant carriers, which is reduced by the superconducting gap. It leads to a tradeoff between a high operation temperature (determined by the indirect coupling) and a short localization length (set by the superconducting gap) of the Majorana bound states. The latter setup, on the other hand, requires a precise control of the chemical potentials in two isolated one-dimensional channels through local voltage gates. These difficulties motivate us to search for a new scheme to avoid fine-tuning of system parameters.

Here we propose a scheme exploiting the recently discovered higher-order topological insulators (HOTIs) [67–74]. Specifically, we focus on three-dimensional helical second-order topological insulators. In contrast to the gapless surface states in their first-order counterparts [6, 7, 75–78], these HOTIs are characterized by helical hinge states, in which opposite spins move in opposite directions, akin to the spin-momentum locked edge channels in quantum spin Hall insulators [79–85]. Important for us, these hinges form one-dimensional channels of identical chemical potentials. There exist compelling experimental evidences for the topological hinge states in Bi(111) nanowires and bilayers [73, 86, 87]. In addition, the observed ballistic supercurrent with nearly perfect transmission indicates good contacts between the hinge states and a superconductor [73, 87], suggesting that bismuth nanowires offer a suitable platform for proximity-induced superconductivity.

tivity.

In this work we make use of the proximity effect in the helical hinges of a HOTI, where two types of pairing gaps arise, one being the local pairing and the other nonlocal, or crossed Andreev pairing. From a single-particle Hamiltonian, we demonstrate that Majorana Kramers pairs (MKPs) emerge when the crossed Andreev pairing dominates over the local pairing. Then, with the renormalization-group (RG) analysis, we show that a rather weak electron-electron interaction is sufficient to push the system into a regime where the crossed Andreev pairing dominates, thus stabilizing the MKPs at the ends of the HOTI nanowire. We support our effective Hamiltonian method with a supplemental microscopic source-term approach.

*Setup.* We now describe the proposed setup in detail. When two parallel hinges (along  $z$  axis) of a helical HOTI are in contact with an  $s$ -wave superconductor, the Cooper pairs in the superconductor can tunnel into the hinges through two processes. The local (nonlocal) pairing process corresponds to the two partners of a Cooper pair tunneling into the same (different) hinge(s). We denote the setup as *parahelical* (*orthohelical*), when the helicities of the two hinges are *the same* (*opposite*). To be specific, in the parahelical setup, a given spin state (say, spin-down) in the two hinges propagates in the same (say,  $+z$ ) direction, whereas in the orthohelical setup the spin-down states in the two hinges move in the opposite directions. The momentum conservation of the crossed Andreev pairing processes requires the chemical potentials of the two hinges to be the same (opposite) for the parahelical (orthohelical) setup [61]. Importantly, since the hinges of a HOTI are connected through a third hinge, the chemical potentials are identical *without applying local voltage gates*, making the parahelical setup a preferable choice for our purpose.

As a concrete example, we consider the recently discovered HOTI material, a bismuth crystal grown along the (111) axis,<sup>1</sup> which hosts helical hinge states [73]; see the left panel

<sup>1</sup> Even though bismuth is a bulk semimetal, the topologically trivial bulk

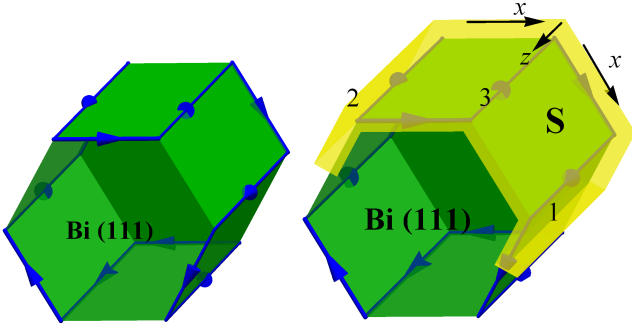


FIG. 1. Left: In a Bi(111) nanowire (green), the gapless states (blue arrows) propagate along the hinges. The spin-up (-down) hinge states move against (along) the directions of the arrows. The helicities of any two parallel hinge states [along  $z \equiv (111)$  axis] on a single lateral facet are opposite. Right: In the proposed setup, a superconducting layer (yellow) is in contact with three parallel hinges (labeled by 1, 2, and 3). The (1,2) pair carries the same helicity, allowing for the crossed Andreev pairing. In contrast, the crossed Andreev pairings between the other pairs [(1,3) and (2,3)] are suppressed; see SM [88]. The  $x$  axis of the local coordinate is defined along the perimeter of the hexagonal cross section, and the  $y$  axis (not shown) is normal to the lateral facets.

of Fig. 1. Since the helicities of any two parallel hinges on the same lateral facet are opposite, the orthohelical setup is realized when a superconductor is placed on one lateral facet, in contact with the two parallel hinges. However, to make the crossed Andreev pairing feasible, the otherwise identical chemical potentials of these hinges would need to be fine-tuned to the opposite through local voltage gates.

Instead of considering this impractical scenario, we turn the limitation on the chemical potential into an advantage. Namely, let us imagine that the superconducting layer extends over two lateral facets, as shown in the right panel of Fig. 1. The superconductor is then in contact with three parallel hinges along  $z \equiv (111)$  axis, two of which (labeled by 1 and 2) carry the same helicity while the third one (labeled by 3) the opposite. The uniform chemical potential (assumed to be in the bulk gap and not very close to the Dirac point) allows the crossed Andreev pairing to occur between the hinge 1 and 2. In contrast, the crossed Andreev pairings between the orthohelical hinges [(1,3) and (2,3) pairs] are suppressed due to the momentum mismatch. The hinge 3 is then decoupled from the remaining two; see Supplemental Material (SM) for the details [88]. As a result, the parahelical setup is realized in the hinges 1 and 2 (see Fig. 2).

*Model.* From now on we focus on the two hinges of interest, which are modeled by the fields,

$$\psi_n(r) = R_{n,\downarrow}(r)e^{ik_F r} + L_{n,\uparrow}(r)e^{-ik_F r}, \quad (1)$$

states can be gapped by, e.g., disorder or finite size [73, 83]. We further note that while we take Bi(111) nanowires as an example, our setup can be implemented as well in other recently predicted helical HOTI materials, such as SnTe, Bi<sub>2</sub>TeI, BiSe, and BiTe [69].

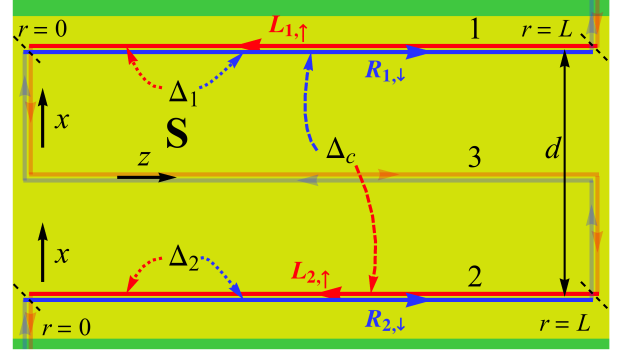


FIG. 2. Schematics of the parahelical setup in the  $xz$  plane of the local coordinate (view from the  $+y$  direction) with the hinge coordinate  $r$ . A superconductor (yellow) is in contact with three long hinges (along  $z$  direction), and several short hinges (along  $x$  direction). The hinges 1 and 2 are separated by a distance  $d$ , where the spin-up states propagate toward the  $-r$  direction (red solid arrows) while the spin-down states toward  $+r$  (blue solid arrows). The hinge 3 is decoupled from the others. The local ( $\Delta_1, \Delta_2$ ) and crossed Andreev ( $\Delta_c$ ) pairing processes are indicated by the dotted and dashed arrows, respectively. Since the short segments are not aligned in the laboratory frame,  $\Delta_c$  is suppressed if  $r \notin [0, L]$ , while  $\Delta_{1,2}$  remains constant for any  $r$ . As a result, the boundaries (black dashed lines) are created at  $r = 0$  and  $r = L$  (the ends of the nanowire), which are assumed to be far away on the scale of the Majorana localization length [88]. For clarity, only one of the crossed Andreev pairing processes,  $\Delta_c R_{1,\downarrow}^\dagger L_{2,\uparrow}^\dagger$ , is shown.

with the coordinate  $r$  along the hinge, the hinge index  $n \in \{1, 2\}$ , the Fermi wave number  $k_F$  (same for the two hinges), and the slowly varying right- and left-moving fields  $R_{n,\downarrow}$  and  $L_{n,\uparrow}$ , respectively. We will suppress the coordinate  $r$  whenever possible, as well as the spin index, the latter being redundant due to the spin-momentum locking. In a noninteracting system, the effective Hamiltonian is given by  $H = H_0 + H_{\text{intra}} + H_c$ , where the kinetic energy term reads

$$H_0 = -i\hbar v_F \sum_{n=1,2} \int dr \left( R_n^\dagger \partial_r R_n - L_n^\dagger \partial_r L_n \right), \quad (2)$$

with the Fermi velocity  $v_F$ . The local pairing term is given by

$$H_{\text{intra}} = \sum_{n=1,2} \int dr \left[ \frac{\Delta_n}{2} (R_n^\dagger L_n^\dagger - L_n^\dagger R_n^\dagger) + \text{H.c.} \right], \quad (3)$$

with the pairing gap  $\Delta_n$  in the hinge  $n$ . The crossed Andreev pairing term is given by

$$H_c = \int dr \left[ \frac{\Delta_c}{2} (R_1^\dagger L_2^\dagger - L_2^\dagger R_1^\dagger) + (1 \leftrightarrow 2) \right] + \text{H.c.}, \quad (4)$$

with the pairing gap  $\Delta_c$ . For simplicity, we take a uniform, real local pairing gap  $\Delta_n > 0$ , while the crossed Andreev pairing gap  $\Delta_c$  changes its (real) value from finite ( $r \in [0, L]$ ) to zero ( $r \notin [0, L]$ ), creating two boundaries at  $r = 0$  and  $r = L$ , as indicated in Fig. 2. We assume the hinge length  $L$

is sufficiently long so that we can focus only on the boundary at  $r = 0$ . Below we will demonstrate the existence of a MKP at such a boundary.

*Majorana Kramers pairs.* We first identify the criterion for the MKPs in a noninteracting system, before moving on to an interacting system. The single-particle Hamiltonian Eqs. (2)–(4) can be written in the basis  $\Psi = (R_1, L_1, R_2, L_2, R_1^\dagger, L_1^\dagger, R_2^\dagger, L_2^\dagger)^T$  as  $H = \frac{1}{2} \int dr \Psi^\dagger(r) \mathcal{H}(r) \Psi(r)$ , with the Hamiltonian density

$$\begin{aligned} \mathcal{H}(r) = & -i\hbar v_F \eta^0 \tau^0 \sigma^z \partial_r - \Delta_+ \eta^y \tau^0 \sigma^y \\ & - \Delta_- \eta^y \tau^z \sigma^y - \Delta_c \eta^y \tau^x \sigma^y, \end{aligned} \quad (5)$$

with  $\Delta_\pm = (\Delta_1 \pm \Delta_2)/2$ . In the above, the matrices  $\eta^\mu$ ,  $\tau^\mu$ , and  $\sigma^\mu$  act on the particle-hole, hinge, and spin space, respectively. They are given by the Pauli (identity) matrix for  $\mu = x, y, z$  ( $\mu = 0$ ). The bulk spectrum is two-fold degenerate due to the time-reversal symmetry, with a gap defined by  $\Delta_b$  (see **SM** for the details [88]). The reversal of the sign of  $\Delta_b$ , which can be shown to coincide with the sign of  $(\Delta_1 \Delta_2 - \Delta_c^2)$ , indicates the band inversion and suggests the presence of zero-energy bound states at a boundary.

It can be shown that such bound states are indeed present by solving the corresponding Bogoliubov-de Gennes equation of Eq. (5) at zero energy. By matching the boundary conditions [58, 89], we find that, when the condition

$$\Delta_c^2 > \Delta_1 \Delta_2 \quad (6)$$

is fulfilled, a MKP emerges at  $r = 0$  (and another pair at  $r = L$ ), with their wave functions given in **SM** [88]. In contrast, when Eq. (6) is violated, the MKPs are absent. We remark that in any realistic setup the change of  $\Delta_c$  will be less abrupt than the step function assumed in our model. Nevertheless, due to their topological origin, the MKP must be present wherever  $\Delta_b$  reverses its sign.

We therefore conclude that the criterion for the MKP is given by Eq. (6), meaning that the crossed Andreev pairing dominates over the local pairing. Whereas Eq. (6) is not fulfilled in a noninteracting system [90], a moderate electron-electron interaction can drive the system into the topological superconducting phase hosting MKPs, as we now demonstrate.

*Interacting system.* First of all, we remark that, since our setup respects the time-reversal symmetry, the elastic backscattering is precluded in the helical channels (unless the time-reversal symmetry is broken by, for example, nuclear spins [91, 92]). We therefore include only the forward scattering processes into the interaction  $H_{\text{int}}$ , and bosonize the hinge total Hamiltonian  $H_{\text{el}} = H_0 + H_{\text{int}}$ . This procedure leads to two copies of the helical Tomonaga-Luttinger liquid,

$$H_{\text{el}} = \sum_{n=1,2} \int \frac{\hbar dr}{2\pi} \left\{ u_n K_n [\partial_r \theta_n(r)]^2 + \frac{u_n}{K_n} [\partial_r \phi_n(r)]^2 \right\}, \quad (7)$$

with the Luttinger liquid parameter  $K_n$  for the hinge  $n$  and the modified velocity  $u_n = v_F/K_n$ . With the boson fields  $\theta_n$

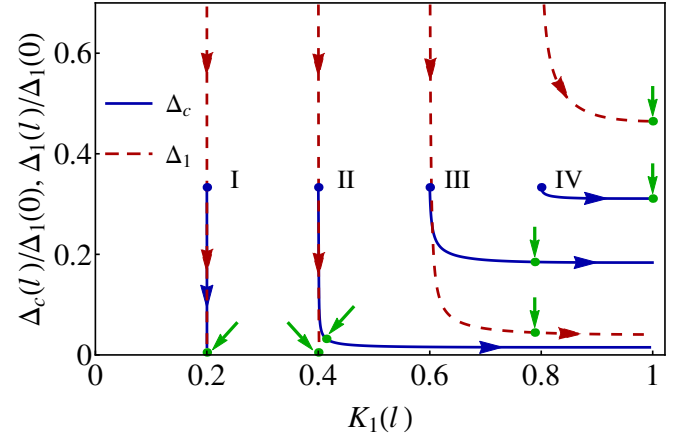


FIG. 3. RG flow diagram. We take the parameters  $K_1(0) = K_2(0) = 0.2, 0.4, 0.6$ , and  $0.8$ ,  $\tilde{\Delta}_1(0) = \tilde{\Delta}_2(0) = 3\tilde{\Delta}_c(0) = 0.03$ ,  $a(0) = 5$  nm, and  $L = 1$   $\mu\text{m}$ . The crossed Andreev (local) pairing gap  $\Delta_c$  ( $\Delta_1 = \Delta_2$ ) is plotted in blue solid (red dashed) curves. The blue dots (labeled by I–IV) mark the initial points of  $\Delta_c$ , and the green arrows and points specify where the RG flows stop. The RG flows labeled by II and III stop at the points at which the renormalized crossed Andreev pairing dominates over the local pairing ( $\Delta_c > \Delta_1$ ), indicating topological superconducting phase.

and  $\phi_n$  given in Eqs. (S14) in **SM** [88], the local pairing term reads

$$H_{\text{intra}} = \sum_{n=1,2} \frac{\Delta_n}{\pi a} \int dr \cos[2\theta_n(r)], \quad (8)$$

where  $a$  is the short-distance cutoff, taken to be the transverse decay length of the hinge states [91, 92]. The crossed Andreev pairing term is

$$H_c = \frac{2\Delta_c}{\pi a} \int dr \cos[\theta_1(r) + \theta_2(r)] \cos[\phi_1(r) - \phi_2(r)]. \quad (9)$$

In the noninteracting limit ( $K_n = 1$ ), the local pairing always dominates. However, we expect that in interacting systems, the crossed Andreev pairing can take over such that the topological criterion [see Eq. (6)] is satisfied.

Next, we derive the RG flow equations following the standard, straightforward procedure [93]. For brevity, we refer to **SM** [88] for the details and only discuss the main results here. To simplify the analysis, we introduce the dimensionless coupling constants,

$$\tilde{\Delta}_1(l) = \frac{\Delta_1(l)a(l)}{\hbar u_1}, \tilde{\Delta}_2(l) = \frac{\Delta_2(l)a(l)}{\hbar u_2}, \tilde{\Delta}_c(l) = \frac{\Delta_c(l)a(l)}{\hbar \sqrt{u_1 u_2}}, \quad (10)$$

with the dimensionless scale  $l = \ln[a(l)/a(0)]$ . For a given set of the initial parameters (at  $l = 0$ ), we numerically propagate the RG flow equations. We stop the RG flow whenever any of the dimensionless coupling constants becomes unity. At these points we obtain the renormalized pairing gaps, allowing us to examine the criterion for the MKP existence.

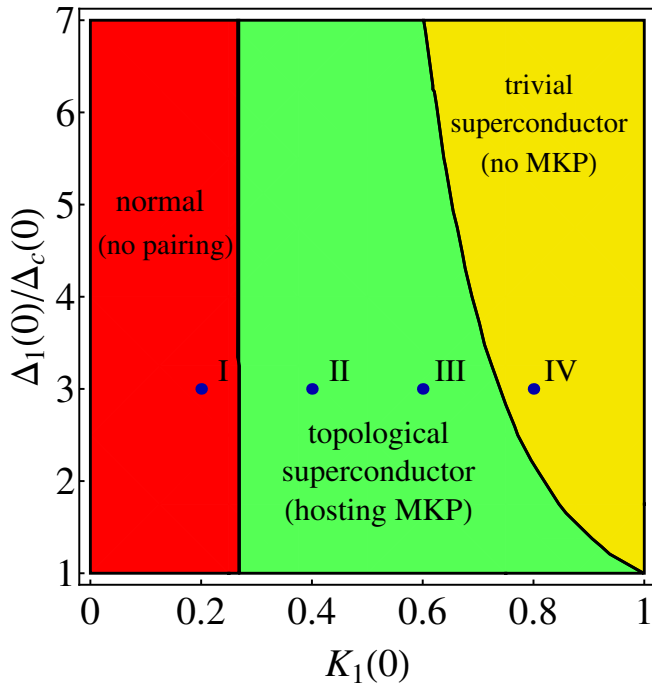


FIG. 4. Phase diagram. The vertical and horizontal axes label the initial values of the gap ratio  $[\Delta_1(0)/\Delta_c(0)]$  and interaction parameter  $K_1(0) = K_2(0)$ , respectively. The other parameters are the same as those in Fig. 3. The green (yellow) region marks the phase with (without) a MKP. The corresponding RG flows to the blue dots (labeled by I–IV) are shown in Fig. 3. In the red region, both types of the pairing gaps vanish.

An example of the RG flow diagram is presented in Fig. 3, showing how the pairing gaps evolve under the flow. The repulsive interaction tends to reduce both types of the pairings. Importantly, due to the local nature of the Coulomb interaction, the local pairing gap (red dashed curve) is suppressed more significantly than the crossed Andreev pairing (blue solid curve), as expected from the different scaling dimensions of the cosine terms in Eqs. (8)–(9); see also Eqs. (S15) in SM [88]. Therefore, the repulsive interaction favors the non-local pairing process. Consequently, even if the initial value of the crossed Andreev pairing gap is smaller than the local pairing gap (we take  $\tilde{\Delta}_c(0)/\tilde{\Delta}_1(0) = 1/3$  in Fig. 3), a sufficiently strong interaction can reverse their relative strengths.

To prove that Eq. (6) with the renormalized pairing gaps is the correct criterion, we note that the end points of the RG flows (indicated by green arrows) are adiabatically connected to the noninteracting limit ( $K_n = 1$ ) without closing the bulk gap again. Here, the model can be refermionized into Eq. (5), with the renormalized pairing gaps [94]. The refermionized model with the renormalized  $\Delta_c$  and  $\Delta_1$  justifies the existence of MKPs. We therefore conclude that a sufficiently strong interaction drives the system into a topological superconducting phase, hosting MKPs.

*Phase diagram.* To investigate the stability of the MKPs in the parameter space, we repeat the above numerical proce-

dures in the regime  $K_1(0) \in [0, 1]$  and  $\Delta_1(0)/\Delta_c(0) \in [1, 7]$ . We present the phase diagram in Fig. 4, where the green (yellow) color marks the region where a MKP is present (absent) at the end of the HOTI nanowire. When the system is noninteracting [ $K_1(0) = 1$ ], the MKPs are absent, consistent with Ref. [90]. However, for a ratio of  $\Delta_1(0)/\Delta_c(0) \geq 1$ , a rather weak interaction  $K_n(0) \lesssim 1$  can stabilize the MKPs. The larger the ratio of  $\Delta_1(0)/\Delta_c(0)$  is, the stronger interaction is required to reverse the gap strengths. A very strong interaction (red region), however, destroys both types of the pairing gaps, as indicated by the RG flow equations; see Eqs. (S15) in SM [88]. Consequently, the hinge channels remains non-superconducting for  $K_1(0) < 2 - \sqrt{3} \approx 0.27$ . In comparison with spin-degenerate nanowires [66], our setup requires weaker interactions for MKPs, making HOTIs a promising platform for topological superconductivity without the need of magnetic fields.

*Discussion.* We further confirm our results with a microscopic model, supplementary to the above effective Hamiltonian method. Such a source-term method is able to capture the effects of the inter-hinge separation  $d$  and the coherence length of the superconductor [66, 95]. The corresponding RG flow equations and phase diagram are given in SM [88], where we show that the crossed Andreev pairing is dominant in the presence of moderate interactions for  $d = 50$  nm. In addition to the MKPs, our setup can also work as a Cooper pair splitter—a source of spatially separated spin-entangled electron pairs [96–105]. Finally, we remark that quantum computation schemes utilizing MKP braiding have been widely discussed in the literature [106, 107]. Our setup provides building blocks for the measurement-based structures proposed in Ref. [108–110], which offers a route to scalable architectures for topological quantum computation.

This work was supported financially by the JSPS Kakenhi Grant No. 16H02204, by the Swiss National Science Foundation (Switzerland), and by the NCCR QSIT. This project received funding from the European Unions Horizon 2020 research and innovation program (ERC Starting Grant, grant agreement No 757725).

- 
- [1] A. Y. Kitaev, Unpaired Majorana fermions in quantum wires, *Phys. Usp.* **44**, 131 (2001).
  - [2] A. Y. Kitaev, Fault-tolerant quantum computation by anyons, *Ann. Phys.* **303**, 2 (2003).
  - [3] C. Nayak, S. H. Simon, A. Stern, M. Freedman, and S. Das Sarma, Non-Abelian anyons and topological quantum computation, *Rev. Mod. Phys.* **80**, 1083 (2008).
  - [4] Y. Tanaka, T. Yokoyama, and N. Nagaosa, Manipulation of the Majorana Fermion, Andreev Reflection, and Josephson Current on Topological Insulators, *Phys. Rev. Lett.* **103**, 107002 (2009).
  - [5] M. Sato and S. Fujimoto, Topological phases of noncentrosymmetric superconductors: Edge states, Majorana fermions, and non-Abelian statistics, *Phys. Rev. B* **79**, 094504 (2009).
  - [6] M. Z. Hasan and C. L. Kane, *Colloquium* : Topological insula-

- tors, *Rev. Mod. Phys.* **82**, 3045 (2010).
- [7] X.-L. Qi and S.-C. Zhang, Topological insulators and superconductors, *Rev. Mod. Phys.* **83**, 1057 (2011).
- [8] J. Alicea, Y. Oreg, G. Refael, F. von Oppen, and M. P. A. Fisher, Non-Abelian statistics and topological quantum information processing in 1D wire networks, *Nat. Phys.* **7**, 412 (2011).
- [9] A. Cook and M. Franz, Majorana fermions in a topological-insulator nanowire proximity-coupled to an *s*-wave superconductor, *Phys. Rev. B* **84**, 201105 (2011).
- [10] J. Klinovaja, P. Stano, and D. Loss, Transition from fractional to Majorana fermions in Rashba nanowires, *Phys. Rev. Lett.* **109**, 236801 (2012).
- [11] D. Chevallier, D. Sticlet, P. Simon, and C. Bena, Mutation of Andreev into Majorana bound states in long superconductor-normal and superconductor-normal-superconductor junctions, *Phys. Rev. B* **85**, 235307 (2012).
- [12] F. Domínguez, F. Hassler, and G. Platero, Dynamical detection of Majorana fermions in current-biased nanowires, *Phys. Rev. B* **86**, 140503 (2012).
- [13] J. Klinovaja, S. Gangadharaiah, and D. Loss, Electric-field-induced majorana fermions in armchair carbon nanotubes, *Phys. Rev. Lett.* **108**, 196804 (2012).
- [14] Y. Niu, S. B. Chung, C.-H. Hsu, I. Mandal, S. Raghu, and S. Chakravarty, Majorana zero modes in a quantum Ising chain with longer-ranged interactions, *Phys. Rev. B* **85**, 035110 (2012).
- [15] E. Prada, P. San-Jose, and R. Aguado, Transport spectroscopy of *NS* nanowire junctions with Majorana fermions, *Phys. Rev. B* **86**, 180503 (2012).
- [16] B. M. Terhal, F. Hassler, and D. P. DiVincenzo, From Majorana fermions to topological order, *Phys. Rev. Lett.* **108**, 260504 (2012).
- [17] C. Beenakker, Search for Majorana Fermions in Superconductors, *Ann. Rev. Condens. Matter Phys.* **4**, 113 (2013).
- [18] K. Björnson and A. M. Black-Schaffer, Vortex states and Majorana fermions in spin-orbit coupled semiconductor-superconductor hybrid structures, *Phys. Rev. B* **88**, 024501 (2013).
- [19] S. Nakosai, J. C. Budich, Y. Tanaka, B. Trauzettel, and N. Nagao, Majorana Bound States and Nonlocal Spin Correlations in a Quantum Wire on an Unconventional Superconductor, *Phys. Rev. Lett.* **110**, 117002 (2013).
- [20] M. Thakurathi, A. A. Patel, D. Sen, and A. Dutta, Floquet generation of Majorana end modes and topological invariants, *Phys. Rev. B* **88**, 155133 (2013).
- [21] E. Dumitrescu, J. D. Sau, and S. Tewari, Magnetic field response and chiral symmetry of time-reversal-invariant topological superconductors, *Phys. Rev. B* **90**, 245438 (2014).
- [22] F. Maier, J. Klinovaja, and D. Loss, Majorana fermions in ge/si hole nanowires, *Phys. Rev. B* **90**, 195421 (2014).
- [23] L. Weithofer, P. Recher, and T. L. Schmidt, Electron transport in multiterminal networks of Majorana bound states, *Phys. Rev. B* **90**, 205416 (2014).
- [24] R. S. Deacon, J. Wiedenmann, E. Bocquillon, F. Domínguez, T. M. Klapwijk, P. Leubner, C. Brüne, E. M. Hankiewicz, S. Tarucha, K. Ishibashi, H. Buhmann, and L. W. Molenkamp, Josephson radiation from gapless Andreev bound states in HgTe-based topological junctions, *Phys. Rev. X* **7**, 021011 (2017).
- [25] G.-Y. Huang and H. Q. Xu, Majorana fermions in topological-insulator nanowires: From single superconducting nanowires to Josephson junctions, *Phys. Rev. B* **95**, 155420 (2017).
- [26] W. Izumida, L. Milz, M. Marganska, and M. Grifoni, Topology and zero energy edge states in carbon nanotubes with superconducting pairing, *Phys. Rev. B* **96**, 125414 (2017).
- [27] J. Manousakis, A. Altland, D. Bagrets, R. Egger, and Y. Ando, Majorana qubits in a topological insulator nanoribbon architecture, *Phys. Rev. B* **95**, 165424 (2017).
- [28] A. Ptok, A. Kobińska, and T. Domański, Controlling the bound states in a quantum-dot hybrid nanowire, *Phys. Rev. B* **96**, 195430 (2017).
- [29] M. Sato and Y. Ando, Topological superconductors: a review, *Rep. Prog. Phys.* **80**, 076501 (2017).
- [30] C. Reeg, D. Loss, and J. Klinovaja, Proximity effect in a two-dimensional electron gas coupled to a thin superconducting layer, *Beilstein J. Nanotechnol.* **9**, 1263 (2018).
- [31] M. Trif, O. Dmytruk, H. Bouchiat, R. Aguado, and P. Simon, Dynamic current susceptibility as a probe of Majorana bound states in nanowire-based Josephson junctions, *Phys. Rev. B* **97**, 041415 (2018).
- [32] R. M. Lutchyn, J. D. Sau, and S. Das Sarma, Majorana Fermions and a Topological Phase Transition in Semiconductor-Superconductor Heterostructures, *Phys. Rev. Lett.* **105**, 077001 (2010).
- [33] Y. Oreg, G. Refael, and F. von Oppen, Helical Liquids and Majorana Bound States in Quantum Wires, *Phys. Rev. Lett.* **105**, 177002 (2010).
- [34] V. Mourik, K. Zuo, S. M. Frolov, S. R. Plissard, E. P. A. M. Bakkers, and L. P. Kouwenhoven, Signatures of Majorana Fermions in Hybrid Superconductor-Semiconductor Nanowire Devices, *Science* **336**, 1003 (2012).
- [35] A. Das, Y. Ronen, Y. Most, Y. Oreg, M. Heiblum, and H. Shtrikman, Zero-bias peaks and splitting in an InAs nanowire topological superconductor as a signature of Majorana fermions, *Nat. Phys.* **8**, 887 (2012).
- [36] M. T. Deng, C. L. Yu, G. Y. Huang, M. Larsson, P. Caroff, and H. Q. Xu, Anomalous Zero-Bias Conductance Peak in a Nb-InSb Nanowire-Nb Hybrid Device, *Nano Lett.* **12**, 6414 (2012).
- [37] L. P. Rokhinson, X. Liu, and J. K. Furdyna, The fractional a.c. Josephson effect in a semiconductor-superconductor nanowire as a signature of Majorana particles, *Nat. Phys.* **8**, 795 (2012).
- [38] A. D. K. Finck, D. J. Van Harlingen, P. K. Mohseni, K. Jung, and X. Li, Anomalous Modulation of a Zero-Bias Peak in a Hybrid Nanowire-Superconductor Device, *Phys. Rev. Lett.* **110**, 126406 (2013).
- [39] H. O. H. Churchill, V. Fatemi, K. Grove-Rasmussen, M. T. Deng, P. Caroff, H. Q. Xu, and C. M. Marcus, Superconductor-nanowire devices from tunneling to the multichannel regime: Zero-bias oscillations and magnetoconductance crossover, *Phys. Rev. B* **87**, 241401 (2013).
- [40] D. Rainis, L. Trifunovic, J. Klinovaja, and D. Loss, Towards a realistic transport modeling in a superconducting nanowire with Majorana fermions, *Phys. Rev. B* **87**, 024515 (2013).
- [41] S. Takei, B. M. Fregoso, H.-Y. Hui, A. M. Lobos, and S. Das Sarma, Soft Superconducting Gap in Semiconductor Majorana Nanowires, *Phys. Rev. Lett.* **110**, 186803 (2013).
- [42] S. M. Albrecht, A. P. Higginbotham, M. Madsen, F. Kuemmeth, T. S. Jespersen, J. Nygård, P. Krogstrup, and C. M. Marcus, Exponential protection of zero modes in Majorana islands, *Nature* **531**, 206 (2016).
- [43] O. Gül, H. Zhang, J. D. S. Bommer, M. W. A. de Moor, D. Car, S. R. Plissard, E. P. A. M. Bakkers, A. Geresdi, K. Watanabe, T. Taniguchi, and L. P. Kouwenhoven, Ballistic Majorana nanowire devices, *Nat. Nanotech.* **13**, 192 (2018).
- [44] H. Zhang, C.-X. Liu, S. Gazibegovic, D. Xu, J. A. Logan, G. Wang, N. van Loo, J. D. S. Bommer, M. W. A. de Moor, D. Car, R. L. M. O. het Veld, P. J. van Veldhoven, S. Koelling,

- M. A. Verheijen, M. Pendharkar, D. J. Pennachio, B. Shojaei, J. S. Lee, C. J. Palmström, E. P. A. M. Bakkers, S. D. Sarma, and L. P. Kouwenhoven, Quantized Majorana conductance, *Nature* **556**, 74 (2018).
- [45] L. Fu and C. L. Kane, Superconducting Proximity Effect and Majorana Fermions at the Surface of a Topological Insulator, *Phys. Rev. Lett.* **100**, 096407 (2008).
- [46] A. Keselman, L. Fu, A. Stern, and E. Berg, Inducing Time-Reversal-Invariant Topological Superconductivity and Fermion Parity Pumping in Quantum Wires, *Phys. Rev. Lett.* **111**, 116402 (2013).
- [47] A. Haim, A. Keselman, E. Berg, and Y. Oreg, Time-reversal-invariant topological superconductivity induced by repulsive interactions in quantum wires, *Phys. Rev. B* **89**, 220504 (2014).
- [48] C. Schrade, A. A. Zyuzin, J. Klinovaja, and D. Loss, Proximity-Induced  $\pi$  Josephson Junctions in Topological Insulators and Kramers Pairs of Majorana Fermions, *Phys. Rev. Lett.* **115**, 237001 (2015).
- [49] C. L. M. Wong and K. T. Law, Majorana Kramers doublets in  $d_{x^2-y^2}$ -wave superconductors with Rashba spin-orbit coupling, *Phys. Rev. B* **86**, 184516 (2012).
- [50] F. Zhang, C. L. Kane, and E. J. Mele, Time-Reversal-Invariant Topological Superconductivity and Majorana Kramers Pairs, *Phys. Rev. Lett.* **111**, 056402 (2013).
- [51] S. Hoffman, J. Klinovaja, and D. Loss, Topological phases of inhomogeneous superconductivity, *Phys. Rev. B* **93**, 165418 (2016).
- [52] J. Klinovaja, P. Stano, A. Yazdani, and D. Loss, Topological superconductivity and Majorana fermions in RKKY systems, *Phys. Rev. Lett.* **111**, 186805 (2013).
- [53] B. Braunecker and P. Simon, Interplay between Classical Magnetic Moments and Superconductivity in Quantum One-Dimensional Conductors: Toward a Self-Sustained Topological Majorana Phase, *Phys. Rev. Lett.* **111**, 147202 (2013).
- [54] M. M. Vazifeh and M. Franz, Self-Organized Topological State with Majorana Fermions, *Phys. Rev. Lett.* **111**, 206802 (2013).
- [55] S. Nadj-Perge, I. K. Drozdov, B. A. Bernevig, and A. Yazdani, Proposal for realizing Majorana fermions in chains of magnetic atoms on a superconductor, *Phys. Rev. B* **88**, 020407 (2013).
- [56] S. Nadj-Perge, I. K. Drozdov, J. Li, H. Chen, S. Jeon, J. Seo, A. H. MacDonald, B. A. Bernevig, and A. Yazdani, Observation of Majorana fermions in ferromagnetic atomic chains on a superconductor, *Science* **346**, 602 (2014).
- [57] F. Pientka, L. I. Glazman, and F. von Oppen, Unconventional topological phase transitions in helical Shiba chains, *Phys. Rev. B* **89**, 180505 (2014).
- [58] C.-H. Hsu, P. Stano, J. Klinovaja, and D. Loss, Antiferromagnetic nuclear spin helix and topological superconductivity in  $^{13}\text{C}$  nanotubes, *Phys. Rev. B* **92**, 235435 (2015).
- [59] R. Pawlak, M. Kisiel, J. Klinovaja, T. Meier, S. Kawai, T. Glatzel, D. Loss, and E. Meyer, Probing atomic structure and Majorana wavefunctions in monoatomic Fe chains on superconducting Pb surface, *npj Quantum Information* **2**, 16035 (2016).
- [60] E. Gaidamauskas, J. Paaske, and K. Flensberg, Majorana Bound States in Two-Channel Time-Reversal-Symmetric Nanowire Systems, *Phys. Rev. Lett.* **112**, 126402 (2014).
- [61] J. Klinovaja, A. Yacoby, and D. Loss, Kramers pairs of Majorana fermions and parafermions in fractional topological insulators, *Phys. Rev. B* **90**, 155447 (2014).
- [62] J. Klinovaja and D. Loss, Time-reversal invariant parafermions in interacting Rashba nanowires, *Phys. Rev. B* **90**, 045118 (2014).
- [63] J. Klinovaja and D. Loss, Fractional charge and spin states in topological insulator constrictions, *Phys. Rev. B* **92**, 121410 (2015).
- [64] H. Ebisu, B. Lu, J. Klinovaja, and Y. Tanaka, Theory of time-reversal topological superconductivity in double Rashba wires: symmetries of Cooper pairs and Andreev bound states, *Prog. Theo. Exp. Phys.* **2016**, 083101 (2016).
- [65] C. Schrade, M. Thakurathi, C. Reeg, S. Hoffman, J. Klinovaja, and D. Loss, Low-field topological threshold in Majorana double nanowires, *Phys. Rev. B* **96**, 035306 (2017).
- [66] M. Thakurathi, P. Simon, I. Mandal, J. Klinovaja, and D. Loss, Majorana Kramers pairs in Rashba double nanowires with interactions and disorder, *Phys. Rev. B* **97**, 045415 (2018).
- [67] W. A. Benalcazar, B. A. Bernevig, and T. L. Hughes, Quantized electric multipole insulators, *Science* **357**, 61 (2017).
- [68] W. A. Benalcazar, B. A. Bernevig, and T. L. Hughes, Electric multipole moments, topological multipole moment pumping, and chiral hinge states in crystalline insulators, *Phys. Rev. B* **96**, 245115 (2017).
- [69] F. Schindler, A. M. Cook, M. G. Vergniory, Z. Wang, S. S. P. Parkin, B. A. Bernevig, and T. Neupert, Higher-Order Topological Insulators, *ArXiv e-prints* (2017), arXiv:1708.03636 [cond-mat.mes-hall].
- [70] J. Langbehn, Y. Peng, L. Trifunovic, F. von Oppen, and P. W. Brouwer, Reflection-Symmetric Second-Order Topological Insulators and Superconductors, *Phys. Rev. Lett.* **119**, 246401 (2017).
- [71] Z. Song, Z. Fang, and C. Fang,  $(d-2)$ -Dimensional Edge States of Rotation Symmetry Protected Topological States, *Phys. Rev. Lett.* **119**, 246402 (2017).
- [72] M. Ezawa, Higher-Order Topological Insulators and Semimetals on the Breathing Kagome and Pyrochlore Lattices, *Phys. Rev. Lett.* **120**, 026801 (2018).
- [73] F. Schindler, Z. Wang, M. G. Vergniory, A. M. Cook, A. Murani, S. Sengupta, A. Y. Kasumov, R. Deblock, S. Jeon, I. Drozdov, H. Bouchiat, S. Guéron, A. Yazdani, B. A. Bernevig, and T. Neupert, Higher-Order Topology in Bismuth, *ArXiv e-prints* (2018), arXiv:1802.02585 [cond-mat.mtrl-sci].
- [74] E. Khalaf, Higher-order topological insulators and superconductors protected by inversion symmetry, *Phys. Rev. B* **97**, 205136 (2018).
- [75] L. Fu, C. L. Kane, and E. J. Mele, Topological Insulators in Three Dimensions, *Phys. Rev. Lett.* **98**, 106803 (2007).
- [76] J. E. Moore and L. Balents, Topological invariants of time-reversal-invariant band structures, *Phys. Rev. B* **75**, 121306 (2007).
- [77] D. Hsieh, D. Qian, L. Wray, Y. Xia, Y. S. Hor, R. J. Cava, and M. Z. Hasan, A topological Dirac insulator in a quantum spin Hall phase, *Nature* **452**, 970 (2008).
- [78] R. Roy, Topological phases and the quantum spin Hall effect in three dimensions, *Phys. Rev. B* **79**, 195322 (2009).
- [79] C. L. Kane and E. J. Mele,  $\mathbb{Z}_2$  topological order and the quantum spin Hall effect, *Phys. Rev. Lett.* **95**, 146802 (2005).
- [80] C. L. Kane and E. J. Mele, Quantum Spin Hall Effect in Graphene, *Phys. Rev. Lett.* **95**, 226801 (2005).
- [81] B. A. Bernevig and S.-C. Zhang, Quantum Spin Hall Effect, *Phys. Rev. Lett.* **96**, 106802 (2006).
- [82] B. A. Bernevig, T. L. Hughes, and S.-C. Zhang, Quantum Spin Hall Effect and Topological Phase Transition in HgTe Quantum Wells, *Science* **314**, 1757 (2006).
- [83] S. Murakami, Quantum Spin Hall Effect and Enhanced Magnetic Response by Spin-Orbit Coupling, *Phys. Rev. Lett.* **97**, 236805 (2006).
- [84] C. Liu, T. L. Hughes, X.-L. Qi, K. Wang, and S.-C. Zhang, Quantum Spin Hall Effect in Inverted Type-II Semiconductors,



- Phys. Rev. Lett. **100**, 236601 (2008).
- [85] M. Wada, S. Murakami, F. Freimuth, and G. Bihlmayer, Localized edge states in two-dimensional topological insulators: Ultrathin Bi films, Phys. Rev. B **83**, 121310 (2011).
  - [86] I. K. Drozdov, A. Alexandradinata, S. Jeon, S. Nadj-Perge, H. Ji, R. J. Cava, B. A. Bernevig, and A. Yazdani, One-dimensional topological edge states of bismuth bilayers, Nat. Phys. **10**, 664 (2014).
  - [87] A. Murani, A. Kasumov, S. Sengupta, Y. A. Kasumov, V. T. Volkov, I. I. Khodos, F. Brisset, R. Delagrangé, A. Chepelianskii, R. Deblock, H. Bouchiat, and S. Guéron, Ballistic edge states in Bismuth nanowires revealed by SQUID interferometry, Nat. Commun. **8**, 15941 (2017).
  - [88] See Supplemental Material at [URL will be inserted by publisher] for the technical details.
  - [89] J. Klinovaja and D. Loss, Composite Majorana fermion wave functions in nanowires, Phys. Rev. B **86**, 085408 (2012).
  - [90] C. Reeg, J. Klinovaja, and D. Loss, Destructive interference of direct and crossed Andreev pairing in a system of two nanowires coupled via an  $s$ -wave superconductor, Phys. Rev. B **96**, 081301 (2017).
  - [91] C.-H. Hsu, P. Stano, J. Klinovaja, and D. Loss, Nuclear-spin-induced localization of edge states in two-dimensional topological insulators, Phys. Rev. B **96**, 081405 (2017).
  - [92] C.-H. Hsu, P. Stano, J. Klinovaja, and D. Loss, Effects of nuclear spins on the transport properties of the edge of two-dimensional topological insulators, Phys. Rev. B **97**, 125432 (2018).
  - [93] T. Giamarchi, *Quantum Physics in One Dimension* (Oxford University Press, New York, 2003).
  - [94] S. Gangadharaiah, B. Braunecker, P. Simon, and D. Loss, Majorana Edge States in Interacting One-Dimensional Systems, Phys. Rev. Lett. **107**, 036801 (2011).
  - [95] P. Virtanen and P. Recher, Signatures of Rashba spin-orbit interaction in the superconducting proximity effect in helical Luttinger liquids, Phys. Rev. B **85**, 035310 (2012).
  - [96] C. Bena, S. Vishveshwara, L. Balents, and M. P. A. Fisher, Quantum Entanglement in Carbon Nanotubes, Phys. Rev. Lett. **89**, 037901 (2002).
  - [97] L. Hofstetter, S. Csonka, J. Nygård, and C. Schönenberger, Cooper pair splitter realized in a two-quantum-dot Y-junction, Nature **461**, 960 (2009).
  - [98] K. Sato, D. Loss, and Y. Tserkovnyak, Cooper-Pair Injection into Quantum Spin Hall Insulators, Phys. Rev. Lett. **105**, 226401 (2010).
  - [99] L. Hofstetter, S. Csonka, A. Baumgartner, G. Fülöp, S. d'Hollosy, J. Nygård, and C. Schönenberger, Finite-Bias Cooper Pair Splitting, Phys. Rev. Lett. **107**, 136801 (2011).
  - [100] J. Schindele, A. Baumgartner, and C. Schönenberger, Near-Unity Cooper Pair Splitting Efficiency, Phys. Rev. Lett. **109**, 157002 (2012).
  - [101] A. Das, Y. Ronen, M. Heiblum, D. Mahalu, A. V. Kretinin, and H. Shtrikman, High-efficiency Cooper pair splitting demonstrated by two-particle conductance resonance and positive noise cross-correlation, Nat. Commun. **3**, 1165 (2012).
  - [102] G. Fülöp, S. d'Hollosy, A. Baumgartner, P. Makk, V. A. Guzenko, M. H. Madsen, J. Nygård, C. Schönenberger, and S. Csonka, Local electrical tuning of the nonlocal signals in a Cooper pair splitter, Phys. Rev. B **90**, 235412 (2014).
  - [103] G. Fülöp, F. Domínguez, S. d'Hollosy, A. Baumgartner, P. Makk, M. H. Madsen, V. A. Guzenko, J. Nygård, C. Schönenberger, A. Levy Yeyati, and S. Csonka, Magnetic Field Tuning and Quantum Interference in a Cooper Pair Splitter, Phys. Rev. Lett. **115**, 227003 (2015).
  - [104] R. S. Deacon, A. Oiwa, J. Sailer, S. Baba, Y. Kanai, K. Shibata, K. Hirakawa, and S. Tarucha, Cooper pair splitting in parallel quantum dot Josephson junctions, Nat. Commun. **6**, 7446 (2015).
  - [105] S. Baba, C. Jünger, S. Matsuo, A. Baumgartner, Y. Sato, H. Kamata, K. Li, S. Jeppesen, L. Samuelson, H. Xu, C. Schönenberger, and S. Tarucha, Cooper-pair splitting in two parallel InAs nanowires, ArXiv e-prints (2018), arXiv:1802.08059 [cond-mat.mes-hall].
  - [106] X.-J. Liu, C. L. M. Wong, and K. T. Law, Non-Abelian Majorana Doublets in Time-Reversal-Invariant Topological Superconductors, Phys. Rev. X **4**, 021018 (2014).
  - [107] P. Gao, Y.-P. He, and X.-J. Liu, Symmetry-protected non-Abelian braiding of Majorana Kramers pairs, Phys. Rev. B **94**, 224509 (2016).
  - [108] L. A. Landau, S. Plugge, E. Sela, A. Altland, S. M. Albrecht, and R. Egger, Towards Realistic Implementations of a Majorana Surface Code, Phys. Rev. Lett. **116**, 050501 (2016).
  - [109] S. Hoffman, C. Schrade, J. Klinovaja, and D. Loss, Universal quantum computation with hybrid spin-Majorana qubits, Phys. Rev. B **94**, 045316 (2016).
  - [110] T. Karzig, C. Knapp, R. M. Lutchyn, P. Bonderson, M. B. Hastings, C. Nayak, J. Alicea, K. Flensberg, S. Plugge, Y. Oreg, C. M. Marcus, and M. H. Freedman, Scalable designs for quasiparticle-poisoning-protected topological quantum computation with majorana zero modes, Phys. Rev. B **95**, 235305 (2017).

# Supplemental Material to “Majorana Kramers pairs in higher-order topological insulators”

Chen-Hsuan Hsu<sup>1</sup>, Peter Stano<sup>1,2,3</sup>, Jelena Klinovaja<sup>1,4</sup>, and Daniel Loss<sup>1,4</sup>

<sup>1</sup>RIKEN Center for Emergent Matter Science (CEMS), Wako, Saitama 351-0198, Japan

<sup>2</sup>Department of Applied Physics, School of Engineering, University of Tokyo, 7-3-1 Hongo, Bunkyo-ku, Tokyo 113-8656, Japan

<sup>3</sup>Institute of Physics, Slovak Academy of Sciences, 845 11 Bratislava, Slovakia

<sup>4</sup>Department of Physics, University of Basel, Klingelbergstrasse 82, CH-4056 Basel, Switzerland

## DECOUPLING OF THE THIRD PARALLEL HINGE

In this Section we show that the third, middle parallel, hinge is trivially gapped and decoupled from the other hinges (1 and 2). We describe the three hinge states by the fields,

$$\psi_n(r) = \psi_{n,\downarrow}(r) + \psi_{n,\uparrow}(r) \text{ for } n \in \{1, 2, 3\}, \quad (\text{S1a})$$

$$\psi_{n,\uparrow}(r) = L_{n,\uparrow}(r)e^{-ik_F r} \text{ for } n \in \{1, 2\}, \quad (\text{S1b})$$

$$\psi_{n,\downarrow}(r) = R_{n,\downarrow}(r)e^{ik_F r} \text{ for } n \in \{1, 2\}, \quad (\text{S1c})$$

$$\psi_{3,\uparrow}(r) = R_{3,\uparrow}(r)e^{ik_F r}, \quad (\text{S1d})$$

$$\psi_{3,\downarrow}(r) = L_{3,\downarrow}(r)e^{-ik_F r}, \quad (\text{S1e})$$

with the coordinate  $r$  along the hinge, the Fermi wave number  $k_F$ , and the slowly varying right- and left-moving fields  $R_{n,\sigma}$  and  $L_{n,\sigma}$  (the spin index  $\sigma \in \{\uparrow, \downarrow\}$ ), respectively. A Bardeen–Cooper–Schrieffer (BCS) type pairing term between the hinges  $n$  and  $n'$  is in the form of

$$\propto [\psi_{n,\downarrow}^\dagger(-k)\psi_{n',\uparrow}^\dagger(k) + \text{H.c.}], \quad (\text{S2})$$

with the momentum  $k$ , which puts constraints on the momenta and spins of the allowed pairs. Namely, for the electrons to be paired, they must possess zero total momentum and opposite spins. The pairing processes within/between the three helical hinges are sketched in Fig. S1. The local pairing terms ( $n = n'$ ) for hinges 1 and 2 are given by Eq. (3) in the main text, and, for hinge 3, it is given by

$$H_3 = \int dr \left[ \frac{\Delta_3}{2} (R_{3,\uparrow}^\dagger L_{3,\downarrow}^\dagger - L_{3,\downarrow}^\dagger R_{3,\uparrow}^\dagger) + \text{H.c.} \right], \quad (\text{S3})$$

with the local pairing gap  $\Delta_3$ . These terms are indicated by the black dotted arrows in Fig. S1.

On the other hand, the crossed Andreev pairing term ( $n \neq n'$ ) requires more cautions. Due to the identical chemical potential of the hinges, the pairing between the parahelical hinges (1 and 2) is allowed, which is described by the green dashed arrows in Fig. S1 [see Eq. (4) in the main text], whereas the corresponding terms between the hinges 3 and  $n \in \{1, 2\}$  are given by

$$\int dr \left\{ (R_{n,\downarrow}^\dagger R_{3,\uparrow}^\dagger e^{-2ik_F r} + L_{3,\downarrow}^\dagger L_{n,\uparrow}^\dagger e^{2ik_F r}) + \text{H.c.} \right\}. \quad (\text{S4})$$

The integral in Eq. (S4) contains a fast oscillating integrand, and vanishes for  $k_F L \gg 1$ . As a result, the cross Andreev pairing between the third hinge and the others is suppressed due to the momentum mismatch, so we can describe the two subsystems separately. To be specific, we describe the whole

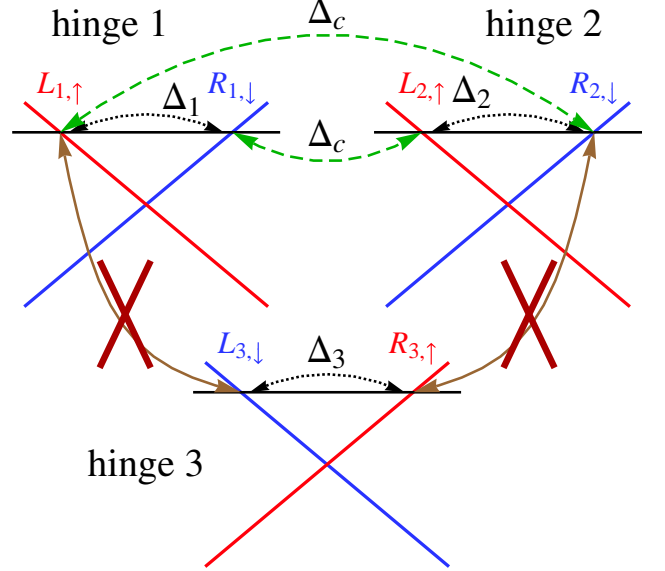


FIG. S1. Schematics of the pairing processes in momentum space. The hinges 1 and 2 carry the same helicity (a given spin state in both of the hinges move in the same direction) while the hinge 3 has the opposite helicity. The local pairing (black dotted arrows,  $\Delta_n$ ) occurs within the hinges. In contrast, the crossed Andreev pairing process (green dashed arrows,  $\Delta_c$ ) is allowed only between the hinges 1 and 2, and forbidden between the other pairs due to the momentum mismatch.

system of the three hinges by the total Hamiltonian,  $H_{\text{tot}} = H + H_3$ , which is block-diagonalized into two parts,

$$H = \frac{1}{2} \int dr \Psi^\dagger(r) \mathcal{H}(r) \Psi(r), \quad (\text{S5a})$$

$$H_3 = \frac{1}{2} \int dr \Psi_3^\dagger(r) \mathcal{H}_3(r) \Psi_3(r), \quad (\text{S5b})$$

with the basis

$$\Psi = (R_{1,\downarrow}, L_{1,\uparrow}, R_{2,\downarrow}, L_{2,\uparrow}, R_{1,\downarrow}^\dagger, L_{1,\uparrow}^\dagger, R_{2,\downarrow}^\dagger, L_{2,\uparrow}^\dagger)^T, \quad (\text{S6a})$$

$$\Psi_3 = (R_{3,\uparrow}, L_{3,\downarrow}, R_{3,\uparrow}^\dagger, L_{3,\downarrow}^\dagger)^T. \quad (\text{S6b})$$

The Hamiltonian density  $\mathcal{H}$  in the subspace of hinges 1 and 2 is given in Eq. (5) in the main text. In the subspace of hinge 3, we have

$$\mathcal{H}_3(r) = -i\hbar v_F \eta^0 \sigma^z \partial_r - \Delta_3 \eta^y \sigma^y, \quad (\text{S7})$$



so the third hinge is trivially gapped by the local pairing, and decoupled from the others. This allows us to focus on two hinges that are parahelical to each other. We therefore present an effective model  $\mathcal{H}$  for the two parahelical hinges of interest (1 and 2) in the main text.

### BULK SPECTRUM AND THE WAVE FUNCTIONS OF THE MAJORANA KRAMERS PAIR

In this Section we give the bulk spectrum of the single-particle Hamiltonian  $\mathcal{H}(r)$  in Eq. (5), and the wave functions of the Majorana Kramers pair localized at the boundary  $r = 0$ , arising from Eq. (5). Upon replacing  $-i\partial_r \rightarrow k$  in  $\mathcal{H}(r)$  and diagonalization, we find the two-fold degenerate bulk spectrum

$$E_{\text{bulk}}^{(\pm, \pm)}(k) = \pm \left[ \hbar^2 v_F^2 k^2 + \left( \Delta_+ \pm \sqrt{\Delta_-^2 + \Delta_c^2} \right)^2 \right]^{1/2}, \quad (\text{S8})$$

which has a gap at  $k = 0$ . To be specific, we define the bulk gap as

$$\begin{aligned} \Delta_b &\equiv E_{\text{bulk}}^{(+, -)}(k=0) - E_{\text{bulk}}^{(-, -)}(k=0) \\ &= 2 \left( \Delta_+ - \sqrt{\Delta_-^2 + \Delta_c^2} \right). \end{aligned} \quad (\text{S9})$$

Assuming  $\Delta_1, \Delta_2 > 0$ , the sign of  $\Delta_b$  is given by the sign of

$$\Delta_1 \Delta_2 - \Delta_c^2, \quad (\text{S10})$$

indicating that the bulk gap  $\Delta_b$  changes its sign when the local and crossed Andreev pairings reverse their relative strengths.

We remark that, for  $\Delta_1$  and  $\Delta_2$  with general signs,  $\Delta_b$  can reverse its sign without involving the crossed Andreev pairing. It can be demonstrated by setting  $\Delta_c = 0$  in Eq. (S9). In this case,  $\Delta_b$  becomes negative when the signs of  $\Delta_1$  and  $\Delta_2$  are opposite ( $\pi$ -junction). The  $\pi$ -junction setup is, however, beyond the scope of the present work [S1–S7]. In the main text, we therefore focus on the case where  $\Delta_1$  and  $\Delta_2$  are both positive.

We now turn to the wave functions of the Majorana Kramers pair. When  $\Delta_c^2 > \Delta_1 \Delta_2$ , we find that a Kramers pair of Majorana bound states emerges at the boundary  $r = 0$ , with the wave functions  $\Phi_{\text{MF},1}$  and  $\Phi_{\text{MF},2}$ . In the basis of  $\Psi = (R_1, L_1, R_2, L_2, R_1^\dagger, L_1^\dagger, R_2^\dagger, L_2^\dagger)^T$  with the transpose operator  $T$ , we have  $\Phi_{\text{MF},1}(r) = \Phi_>(r)\Theta(r) + \Phi_<(r)\Theta(-r)$ , with the step function  $\Theta(r)$  and

$$\Phi_>(r) = e^{-\kappa r} \times (i\eta, -\eta, -i, 1, -i\eta, -\eta, i, 1)^T, \quad (\text{S11a})$$

$$\begin{aligned} \Phi_<(r) = & (i\eta e^{\kappa_1 r}, -\eta e^{\kappa_1 r}, -ie^{\kappa_2 r}, e^{\kappa_2 r}, \\ & -i\eta e^{\kappa_1 r}, -\eta e^{\kappa_1 r}, ie^{\kappa_2 r}, e^{\kappa_2 r})^T, \end{aligned} \quad (\text{S11b})$$

where the normalization constants of  $\Phi_>(r)$  and  $\Phi_<(r)$  were

omitted, and

$$\eta = \frac{\sqrt{\Delta_-^2 + \Delta_c^2} - \Delta_-}{\Delta_c}, \quad (\text{S12a})$$

$$\kappa = \frac{\sqrt{\Delta_-^2 + \Delta_c^2} - \Delta_+}{\hbar v_F}, \quad (\text{S12b})$$

$$\kappa_n = \frac{\Delta_n}{\hbar v_F} \text{ for } n \in \{1, 2\}. \quad (\text{S12c})$$

The localization length of the Majorana bound states is thus given by

$$\xi_{\text{loc}} = \frac{1}{\min(\kappa, \kappa_1, \kappa_2)}, \quad (\text{S13})$$

which is estimated in the following section. The second Majorana wave function is related to its Kramers partner by  $\Phi_{\text{MF},2} = \mathcal{T}\Phi_{\text{MF},1}$  with the time-reversal operator  $\mathcal{T} = i\sigma^y \mathcal{K}$  and the complex conjugate operator  $\mathcal{K}$ . We note that the two Majorana wave functions also satisfy the relation  $\Phi_{\text{MF},1} = -\mathcal{T}\Phi_{\text{MF},2}$ , such that  $\mathcal{T}^2 = -1$ , as required for spin-1/2 particles. One can check that  $\Phi_{\text{MF},1}$  and  $\Phi_{\text{MF},2}$  are orthogonal, as guaranteed by the Kramers degeneracy theorem. Therefore, even though they are not spatially separated, they do not hybridize into an ordinary fermion as long as time-reversal symmetry is preserved.

### BOSONIZATION

In this supplemental section we introduce the boson fields  $\theta_n$  and  $\phi_n$  used to bosonize the Hamiltonian in an interacting system. They are related to the fermion fields  $R_n$  and  $L_n$  through (with the hinge index  $n \in \{1, 2\}$ )

$$R_n(r) = \frac{U_R}{\sqrt{2\pi a}} e^{i[-\phi_n(r) + \theta_n(r)]}, \quad (\text{S14a})$$

$$L_n(r) = \frac{U_L}{\sqrt{2\pi a}} e^{i[\phi_n(r) + \theta_n(r)]}, \quad (\text{S14b})$$

where  $U_R$  and  $U_L$  are the Klein factors, and  $a$  is the short-distance cutoff, taken to be the transverse decay length of the hinge states. The formulas (S14) are used to derive Eqs. (7), (8), and (9) in the main text.

### RG FLOW EQUATIONS DERIVED FROM THE EFFECTIVE HAMILTONIAN METHOD

In this Section we give the renormalization-group (RG) flow equations derived by using the effective Hamiltonian method [see Eqs. (7), (8), and (9) in the main text]. Since Eq. (9) contains the fields  $\phi_n$  while Eq. (8) contains their conjugate fields  $\theta_n$ , the two types of pairing processes compete with each other [S8]. We then expect that their relative strength varies with the interaction strength, as we demonstrate below.

We construct the RG flow equations by computing the correlation function, and changing the cutoff  $a \rightarrow a(l) = a(0)e^l$  [S8], which leads to

$$\frac{d\tilde{\Delta}_1(l)}{dl} = \left[2 - \frac{1}{K_1(l)}\right] \tilde{\Delta}_1(l), \quad (\text{S15a})$$

$$\frac{d\tilde{\Delta}_2(l)}{dl} = \left[2 - \frac{1}{K_2(l)}\right] \tilde{\Delta}_2(l), \quad (\text{S15b})$$

$$\frac{d\tilde{\Delta}_c(l)}{dl} = \left[2 - \frac{1}{4} \left(K_1(l) + K_2(l) + \frac{1}{K_1(l)} + \frac{1}{K_2(l)}\right)\right] \times \tilde{\Delta}_c(l), \quad (\text{S15c})$$

$$\frac{dK_1(l)}{dl} = \tilde{\Delta}_1^2(l) + \frac{1}{2} [1 - K_1^2(l)] \tilde{\Delta}_c^2(l), \quad (\text{S15d})$$

$$\frac{dK_2(l)}{dl} = \tilde{\Delta}_2^2(l) + \frac{1}{2} [1 - K_2^2(l)] \tilde{\Delta}_c^2(l), \quad (\text{S15e})$$

where the dimensionless coupling constants are given by

$$\tilde{\Delta}_1(l) = \frac{\Delta_1(l)a(l)}{\hbar u_1}, \quad \tilde{\Delta}_2(l) = \frac{\Delta_2(l)a(l)}{\hbar u_2}, \quad (\text{S16a})$$

$$\tilde{\Delta}_c(l) = \frac{\Delta_c(l)a(l)}{\hbar \sqrt{u_1 u_2}}. \quad (\text{S16b})$$

Several remarks on Eqs. (S15) are in order. First, both types of dimensionful pairing gaps  $\Delta_n$  and  $\Delta_c$  are suppressed by a repulsive interaction  $K_n(0) < 1$ . Second, due to the different scaling dimensions of the cosine terms in Eqs. (8)–(9), the local pairing gap is suppressed more significantly than the crossed Andreev pairing. Therefore, the repulsive interaction favors the nonlocal pairing process, similarly as in nonhelical nanowires [S9]. Third, from Eqs. (S15), we see that, for  $K_1(0) = K_2(0) < 2 - \sqrt{3} \approx 0.27$ , both  $\tilde{\Delta}_{1,2}$  and  $\tilde{\Delta}_c$  are irrelevant in the RG sense. Namely, both of the gaps flow to zero, so the hinge states remain non-superconducting in the presence of a very strong electron-electron interaction.

The RG flow equations Eqs. (S15) are numerically solved using the initial conditions,

$$\tilde{\Delta}_1(0) \equiv \tilde{\Delta}_1(l=0) = \tilde{\Delta}_2(l=0), \quad (\text{S17a})$$

$$\tilde{\Delta}_c(0) \equiv \tilde{\Delta}_c(l=0), \quad (\text{S17b})$$

$$K_1(0) \equiv K_1(l=0) = K_2(l=0). \quad (\text{S17c})$$

The RG flow is stopped whenever any of the dimensionless coupling constants becomes unity, including also the interaction parameters  $K_n$  and the dimensionless system size  $\ln[L/a(0)]$  with the hinge length  $L$ . The main results of the numerical calculation are presented in Figs. 3 and 4 as well as they are discussed in the main text. Moreover, the renormalized values of the pairing gaps allow us to obtain the localization length. Using Eq. (S13) and the initial parameters  $K_1(0) = K_2(0) = 0.6\text{--}0.7$ ,  $\tilde{\Delta}_1(0) = \tilde{\Delta}_2(0) = 0.03$ ,  $\tilde{\Delta}_c(0) = 0.01$ , and  $a(0) = 5$  nm, we get  $\xi_{\text{loc}} = 19\text{--}21$  nm, which is much shorter than the hinge length  $L \sim O(\mu\text{m})$ , and justifies that the Majorana bound states located at  $r = 0$  and  $r = L$  do not overlap.

## SOURCE-TERM APPROACH

In this Section we present the RG flow equations and phase diagram obtained from the source-term approach [S9, S10], supplementary to the effective Hamiltonian method presented in the main text. We assume a weak tunnel coupling between the hinge states and a proximity BCS superconductor, described by the tunnel Hamiltonian

$$H_T = \sum_{n=1,2} \int dr d\mathbf{R} \left\{ t'_n(r, \mathbf{R}) \left[ R_n^\dagger(r) \psi_{s,\downarrow}(\mathbf{R}) + L_n^\dagger(r) \psi_{s,\uparrow}(\mathbf{R}) \right] + \text{H.c.} \right\}. \quad (\text{S18})$$

Here,  $\mathbf{R}$  is the three-dimensional coordinate in the bulk of the superconductor, and  $\psi_{s,\sigma}$  is the annihilation operator with spin  $\sigma$  in the superconductor. We take the tunnel amplitude  $t'_n$  to be in the form of the three-dimensional delta function,

$$t'_n(r, \mathbf{R}) \equiv t_n \delta(R_z - r) \delta(R_x - d_n) \delta(R_y), \quad (\text{S19a})$$

with  $d_1 = d/2$  and  $d_2 = -d/2$ , where  $d$  is the distance between the two hinges. The BCS Hamiltonian describing the superconductor is given by

$$H_{\text{BCS}} = \sum_{\mathbf{k}, \sigma=\uparrow, \downarrow} \frac{\hbar^2(k^2 - k_{F,s}^2)}{2m_e} \psi_{s,\sigma}^\dagger(\mathbf{k}) \psi_{s,\sigma}(\mathbf{k}) + \Delta_s \sum_{\mathbf{k}} \psi_{s,\uparrow}(\mathbf{k}) \psi_{s,\downarrow}(-\mathbf{k}) + \text{H.c.}, \quad (\text{S20})$$

with the electron mass  $m_e$ , the BCS pairing gap  $\Delta_s$ , and the Fermi wave number  $k_{F,s}$  of the superconductor in its normal phase.

To proceed, we first integrate out the field  $\psi_{s,\sigma}$  in  $H_{\text{BCS}} + H_T$  to obtain the effective action [S11], and then construct the RG flow equations following Refs. [S8–S10]. The result is summarized as follows,

$$\frac{d\tilde{t}_1(l)}{dl} = \left[2 - \frac{1}{4} \left(K_1(l) + \frac{1}{K_1(l)}\right)\right] \tilde{t}_1(l), \quad (\text{S21a})$$

$$\frac{d\tilde{t}_2(l)}{dl} = \left[2 - \frac{1}{4} \left(K_2(l) + \frac{1}{K_2(l)}\right)\right] \tilde{t}_2(l), \quad (\text{S21b})$$

$$\frac{d\tilde{\Delta}_1(l)}{dl} = \left[2 - \frac{1}{K_1(l)}\right] \tilde{\Delta}_1(l) + S_1(l) \tilde{t}_1^2(l), \quad (\text{S21c})$$

$$\frac{d\tilde{\Delta}_2(l)}{dl} = \left[2 - \frac{1}{K_2(l)}\right] \tilde{\Delta}_2(l) + S_2(l) \tilde{t}_2^2(l), \quad (\text{S21d})$$

$$\frac{d\tilde{\Delta}_c(l)}{dl} = \left[2 - \frac{1}{4} \left(K_1(l) + K_2(l) + \frac{1}{K_1(l)} + \frac{1}{K_2(l)}\right)\right] \times \tilde{\Delta}_c(l) + S_c(l) \tilde{t}_1(l) \tilde{t}_2(l), \quad (\text{S21e})$$

$$\frac{dK_1(l)}{dl} = \tilde{\Delta}_1^2(l) + \frac{1}{2} [1 - K_1^2(l)] \tilde{\Delta}_c^2(l), \quad (\text{S21f})$$

$$\frac{dK_2(l)}{dl} = \tilde{\Delta}_2^2(l) + \frac{1}{2} [1 - K_2^2(l)] \tilde{\Delta}_c^2(l), \quad (\text{S21g})$$

where the dimensionless coupling constants for the pairing gaps are given in Eqs. (S16), and the dimensionless tunnel

amplitude is given by

$$\tilde{t}_n(l) = t_n(l) \sqrt{\frac{a^3(l)}{\hbar^2 u_n^2 \xi_s^2 L}}, \quad (\text{S22})$$

with the hinge length  $L$  and the coherence length  $\xi_s$  of the superconductor. The coefficients of the source terms are given by

$$S_n(l) = \frac{m_e v_{Fs}^2 L}{2\pi \Delta_s a(l)} K_0\left(\frac{\Delta_s a(l)}{\hbar u_n}\right), \quad (\text{S23a})$$

$$S_c(l) = \frac{m_e v_{Fs}^2 L}{2\pi \Delta_s d} e^{-d/\xi_s} |\sin(k_{Fs} d)| \times I_0\left(\frac{\Delta_s a(l)}{2\hbar \sqrt{u_1 u_2}}\right) K_0\left(\frac{\Delta_s a(l)}{2\hbar \sqrt{u_1 u_2}}\right), \quad (\text{S23b})$$

with the modified Bessel function of the first- (second-) kind,  $I_0(x)$  [ $K_0(x)$ ]. The behavior of Eqs. (S23) is discussed in Ref. [S9], so not repeated here. Rather, we point out that the source terms naturally include the effects of the coherence length and the distance  $d$  between the hinges. Namely, due to the factor  $e^{-d/\xi_s} |\sin(k_{Fs} d)| \xi_s/d$ , the strength of the crossed Andreev pairing is reduced when the distance  $d$  increases [S11]. In contrast, in the effective Hamiltonian model, such a dependence is not explicitly included, and has to be incorporated by setting an initial ratio  $\Delta_c(0)/\Delta_1(0) < 1$ . Nonetheless, as demonstrated below, our numerical calculation show that such a reduction is modest for a small ratio of  $d/\xi_s$ , so the crossed Andreev pairing can eventually dominate over the local pairing in the presence of interactions.

The RG flow equations Eqs. (S21) are numerically solved along with the following initial parameter values

$$\tilde{t}_1(0) \equiv \tilde{t}_1(l=0) = \tilde{t}_2(l=0), \quad (\text{S24a})$$

$$K_1(0) \equiv K_1(l=0) = K_2(l=0), \quad (\text{S24b})$$

$$S_1(0) \equiv S_1(l=0) = S_2(l=0), \quad (\text{S24c})$$

$$S_c(0) \equiv S_c(l=0), \quad (\text{S24d})$$

$$\tilde{\Delta}_1(l=0) = \tilde{\Delta}_2(l=0) = 0, \quad (\text{S24e})$$

$$\tilde{\Delta}_c(0) = \tilde{\Delta}_c(l=0) = 0. \quad (\text{S24f})$$

This means that the initial values of the pairing gaps are set to zero. Under the RG flow, the pairing gaps are induced by the source terms arising from the tunnel Hamiltonian [see Eq. (S18)]. We obtain the phase diagram by solving Eqs. (S21) with the initial parameters [see Eqs. (S24)] in the regime  $K_1(0) \in [0, 1]$  and  $\Delta_{t0}/\Delta_s \in [0.1, 1]$ , as displayed in Fig. S2. The result is qualitatively similar to the one obtained from the effective Hamiltonian method. Crucially, the result demonstrates that, when the distance between the hinges is  $d = 50$  nm, the Majorana Kramers pair is stabilized in a wide regime in the parameter space. In addition, we also check the phase diagrams with  $d = 100$  nm and  $200$  nm (not shown), and find no qualitative difference among  $d = 50$  nm,  $d = 100$  nm, and  $d = 200$  nm. The green region where the Majorana Kramers pair is present, however, becomes smaller for a larger separation  $d$ , as expected.

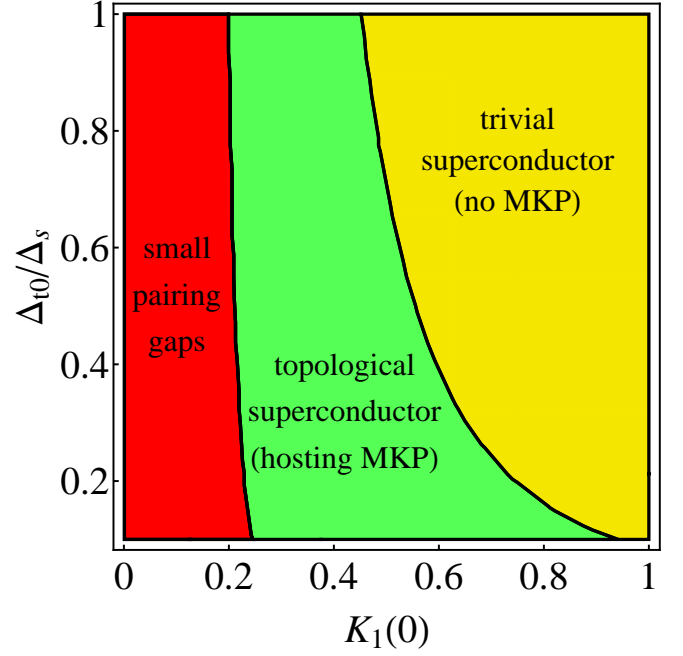


FIG. S2. Phase diagram obtained from the source-term approach, i.e., by solving the RG flow equations in Eqs. (S21). Here we define  $\Delta_{t0} \equiv \tilde{t}_1^2(0) S_1(0) \hbar u_1 / a(0)$ , and take the following parameters:  $u_1 = u_2 = 10^5$  m/s,  $a(0) = 5$  nm,  $L = 1$   $\mu$ m,  $\Delta_s = 0.35$  meV,  $k_{Fs} = 10^{10}$  m $^{-1}$ , and  $d = 50$  nm. As in Fig. 4 in the main text, the green (yellow) region specifies the phase with (without) a Majorana Kramers pair. In the red region, the renormalized values of both  $\tilde{\Delta}_c$  and  $\tilde{\Delta}_1$  are less than 0.1.

As a side remark, in the small  $K_1(0)$  (strongly interacting) regime, the gaps do not flow to exact zero. This is due to the source terms contained in Eqs. (S21). As mentioned above, in contrast to Eqs. (S15), these source terms contribute to the flow equations for  $\tilde{\Delta}_n$  and  $\tilde{\Delta}_c$  in Eqs. (S21). Therefore, in the presence of a strong interaction, the RG flows of these parameters are stopped by the hinge length of  $O(\mu\text{m})$  before going to zero, leading to tiny but finite gaps. In plotting Fig. S2, we therefore label the region in which both the renormalized gaps  $\tilde{\Delta}_c$  and  $\tilde{\Delta}_1$  are less than 0.1 as the “small pairing gaps” region (marked in red color). This region then corresponds to the normal phase (no pairing) in Fig. 4. In conclusion, the source-term approach confirms the results presented in Fig. 4 in the main text.

- 
- [S1] L. Fu and C. L. Kane, Phys. Rev. Lett. **100**, 096407 (2008).
  - [S2] C. L. M. Wong and K. T. Law, Phys. Rev. B **86**, 184516 (2012).
  - [S3] A. Keselman, L. Fu, A. Stern, and E. Berg, Phys. Rev. Lett. **111**, 116402 (2013).
  - [S4] F. Zhang, C. L. Kane, and E. J. Mele, Phys. Rev. Lett. **111**, 056402 (2013).
  - [S5] A. Haim, A. Keselman, E. Berg, and Y. Oreg, Phys. Rev. B **89**, 220504 (2014).

- [S6] C. Schrade, A. A. Zyuzin, J. Klinovaja, and D. Loss, Phys. Rev. Lett. **115**, 237001 (2015).
- [S7] S. Hoffman, J. Klinovaja, and D. Loss, Phys. Rev. B **93**, 165418 (2016).
- [S8] T. Giamarchi, *Quantum Physics in One Dimension* (Oxford University Press, New York, 2003).
- [S9] M. Thakurathi, P. Simon, I. Mandal, J. Klinovaja, and D. Loss, Phys. Rev. B **97**, 045415 (2018).
- [S10] P. Virtanen and P. Recher, Phys. Rev. B **85**, 035310 (2012).
- [S11] C. Reeg, J. Klinovaja, and D. Loss, Phys. Rev. B **96**, 081301 (2017)